Pharmacokinetic Evaluation of the Tau PET Radiotracer ^{18}F-T807 (^{18}F-AV-1451) in Human Subjects

Dustin W. Wooten[1,2], Nicolas J. Guehl[1,2], Eline E. Verwer[1,2], Timothy M. Shoup[1,2], Daniel L. Yokell[1,2], Nevena Zubcevik[3], Neil Vasdev[1,2], Ross D. Zafonte[3,4], Keith A. Johnson[2], Georges El Fakhri[1,2], and Marc D. Normandin[1,2]

[1]Gordon Center for Medical Imaging, Massachusetts General Hospital, Harvard Medical School, Boston, Massachusetts; [2]Division of Nuclear Medicine and Molecular Imaging, Department of Radiology, Massachusetts General Hospital, Harvard Medical School, Boston, Massachusetts; [3]Department of Physical Medicine and Rehabilitation, Spaulding Rehabilitation Hospital, Massachusetts General Hospital, Boston, Massachusetts; and [4]Brigham and Women's Hospital, Harvard Medical School, Boston, Massachusetts

^{18}F-T807 is a PET radiotracer developed for imaging tau protein aggregates, which are implicated in neurologic disorders including Alzheimer disease and traumatic brain injury (TBI). The current study characterizes ^{18}F-T807 pharmacokinetics in human subjects using dynamic PET imaging and metabolite-corrected arterial input functions. **Methods:** Nine subjects (4 controls, 3 with a history of TBI, 2 with mild cognitive impairment due to suspected Alzheimer disease) underwent dynamic PET imaging for up to 120 min after bolus injection of ^{18}F-T807 with arterial blood sampling. Total volume of distribution (V_T) was estimated using compartmental modeling (1- and 2-tissue configurations) and graphical analysis techniques (Logan and multilinear analysis 1 [MA1] regression methods). Reference region–based methods of quantification were explored including Logan distribution volume ratio (DVR) and static SUV ratio (SUVR) using the cerebellum as a reference tissue. **Results:** The percentage of unmetabolized ^{18}F-T807 in plasma followed a single exponential with a half-life of 17.0 ± 4.2 min. Metabolite-corrected plasma radioactivity concentration fit a biexponential (half-lives, 18.1 ± 5.8 and 2.4 ± 0.5 min). ^{18}F-T807 in gray matter peaked quickly (SUV > 2 at ~5 min). Compartmental modeling resulted in good fits, and the 2-tissue model with estimated blood volume correction (2Tv) performed best, particularly in regions with elevated binding. V_T was greater in mild cognitive impairment subjects than controls in the occipital, parietal, and temporal cortices as well as the posterior cingulate gyrus, precuneus, and mesial temporal cortex. High focal uptake was found in the posterior corpus callosum of a TBI subject. Plots from Logan and MA1 graphical methods became linear by 30 min, yielding regional estimates of V_T in excellent agreement with compartmental analysis and providing high-quality parametric maps when applied in voxelwise fashion. Reference region–based approaches including Logan DVR (t^* = 55 min) and SUVR (80- to 100-min interval) were highly correlated with DVR estimated using 2Tv (R^2 = 0.97, $P < 0.0001$). **Conclusion:** ^{18}F-T807 showed rapid clearance from plasma and properties suitable for tau quantification with PET. Furthermore, simplified approaches using DVR (t^* = 55 min) and static SUVR (80–100 min) with cerebellar reference tissue were found to correlate highly with compartmental modeling outcomes.

Key Words: tau; PET; ^{18}F-T807; pharmacokinetics; kinetic modeling

J Nucl Med 2017; 58:484–491
DOI: 10.2967/jnumed.115.170910

The tubulin-associated unit (or tau) is a naturally occurring protein that is integral in providing the white matter microtubule support structure. When impaired, tau proteins can abnormally hyperphosphorylate to form paired helical filaments and eventually insoluble aggregates (*1,2*). These neuronal changes are believed to cause decline in neuronal communication and eventual cell death. Tau pathology is a key hallmark in Alzheimer disease (*3*) and traumatic brain injury (TBI) (*4,5*). Recently, much effort has been placed in the development of PET radiotracers for in vivo quantitation of tau (*6*). Optimal radiotracer characteristics for quantification of tauopathies include selectivity for tau, low nonspecific uptake, high brain penetration, fast clearance from plasma, minimal brain-penetrating radioactive metabolites, and minimal defluorination for ^{18}F-labeled compounds. Several PET radiotracers are currently in use. ^{18}F-FDDNP showed promise initially, but binding was found to be nonspecific (*7*). In vivo imaging with ^{11}C-PBB3 (*8*) resulted in a radioactive metabolite that was found to enter the brain, complicating quantification of tau pathology (*9*). A series of compounds developed by Okamura et al. are showing potential. Earlier versions, THK5105 and THK5117, had relatively high levels of white matter uptake, however, the most recent compound, THK5351, is reported to exhibit less white matter retention and promising kinetics (*10,11*). Two other compounds were developed by Siemens, namely ^{18}F-T807 (*12,13*) (also known as ^{18}F-AV1451) and ^{18}F-T808 (*14*). ^{18}F-T808 demonstrated high bone uptake suggestive of defluorination (*15*). ^{18}F-T807 showed favorable PET imaging properties, and imaging studies showed ^{18}F-T807 uptake tracked well with expected tau pathology distribution throughout the stages of Alzheimer disease (*12*). Because of the difficult synthesis of ^{18}F-T807 using methods initially described, our group developed a concise radiosynthesis appropriate for production on commercially available automated synthesis modules, expanding the access of ^{18}F-T807 (*16*).

Binding of ^{18}F-T807 in postmortem brain tissue from a range of neurologic conditions has been assessed (*17*), and research using ^{18}F-T807 for in vivo imaging has been active (*18*); however, a full

Received Jan. 6, 2016; revision accepted Aug. 26, 2016.
For correspondence or reprints contact: Marc D. Normandin, Massachusetts General Hospital, 55 Fruit St., White 427, Boston, MA 02114.
E-mail: normandin@mgh.harvard.edu
Published online Sep. 22, 2016.

characterization of the in vivo pharmacokinetic profile and determination of appropriate quantification methods have yet to be performed. Therefore, the goal of this work was to evaluate the pharmacokinetics of ^{18}F-T807 using dynamic PET imaging data and arterial input functions corrected for radiometabolites. In subjects demonstrating a wide range of expected tau pathology including healthy controls, subjects with mild cognitive impairment (MCI), and subjects with a history of TBI, we performed compartmental modeling using arterial input functions. With the compartmental modeling estimates of total volume of distribution (V_T) as a gold standard, we then compared simplified approaches for estimation of V_T and reference region–based methods for quantitation of ^{18}F-T807 uptake.

MATERIALS AND METHODS

Subjects

As shown in Table 1, 9 subjects, consisting of 4 healthy controls absent neurologic conditions, 2 subjects with mild cognitive impairment (MCI), and 3 subjects with a history of TBI (2 due to automotive accidents and 1 former professional football player with history of concussion), were included in this work. The study was approved by the institutional review board at Massachusetts General Hospital, and all subjects signed an informed consent form.

Imaging Procedures

MRI. MRI procedures were performed for acquisition of a structural T1-weighted magnetization-prepared rapid gradient-echo (MPRAGE) (*19*) using a 3-T Tim Trio (Siemens Medical Systems). The 3-dimensional acquisition used the following parameters: repetition time/echo time/inversion time, 2,100/2.89/1,100 ms; flip angle, 12°; slice thickness, 1 mm; matrix size, 256 × 224.

PET. ^{18}F-T807 was synthesized as previously described (*16*). Imaging was performed using an ECAT EXACT HR+ (CTI/Siemens) in 3-dimensional acquisition mode. Emission data collection was initiated with the bolus injection of 121–196 MBq of ^{18}F-T807. Time bins were 6 × 10, 8 × 15, 6 × 30, 8 × 60, 8 × 120, and 6 × 300 s for the first 60 min, at which time subjects were allowed a brief break before being repositioned on the scanner for collection of emission data from 75 up to 120 min in 9 × 300 s frames. Six-minute transmission scans were acquired just before administration of ^{18}F-T807 and immediately after the end of emission data acquisition for attenuation correction of PET images in the first and second scan blocks, respectively. ^{18}F-T807 was administered via the antecubital vein over a 1-min infusion using a Medfusion syringe pump whereas arterial samples were drawn from the radial artery of the opposite arm. Arterial samples of 1–3 mL were acquired every 15 s immediately after radiotracer injection and decreased in frequency to every 15 min toward the end of the scanning duration. ^{18}F-T807 metabolism was measured from 3-mL blood samples acquired at 5, 10, 15, 30, 60, and 90 min.

Data Processing and Analysis

Image Processing. Dynamic PET sinograms were reconstructed using filtered backprojection, and corrections for scatter, attenuation, deadtime, random coincident events, and scanner normalization were applied. Final reconstructed images had voxel dimensions of 128 × 128 × 63 and voxel sizes of 2.06 × 2.06 × 2.42 mm. Motion correction was effected through frame-by-frame rigid body registration using a least-squares algorithm with Levenberg–Marquardt optimization as described by Alpert et al. (*20*).

Dynamic PET images from session 2 were summed and rigidly coregistered to summed images from the prebreak imaging session (part 1). To derive the transformation matrix, the dynamic PET images (summed from 1 to 10 min after ^{18}F-T807 injection) were rigidly coregistered to the structural MPRAGE image and the MPRAGE itself was transformed into standard Montreal Neurological Institute (MNI) space (*21*) using affine registration followed by nonlinear warping (FMRIB's Linear Image Registration Tool [FLIRT] and FMRIB's Non-Linear Image Registration Tool [FNIRT] in FMRIB Software Library [FSL] (*22*)). The combined transformation matrix was then applied inversely on MNI and Harvard-Oxford atlases (FSL) to warp the atlas-based regions of interest into native PET space for extraction of radioactivity time–activity curves. Regions of interest surveyed in this work are described in Supplemental Table 1 (supplemental materials are available at http://jnm.snmjournals.org) and shown in Supplemental Figure 1. To facilitate direct visual comparison between subjects, the PET images shown in the figures were transformed into MNI space using the derived combined transformation matrix.

Arterial Input Function. Whole-blood and plasma time–activity curves were obtained by linear interpolation of radioactivity concentrations

TABLE 1
Subject Information

Subject no.	Status	Age (y)	Sex	Mass (kg)	Body mass index (kg/m^2)	Years since TBI exposure
1	CNTL	60	M	93	28.5	NA
2	CNTL	29	M	74	22.2	NA
3	CNTL	47	M	136	38.5	NA
4	CNTL	53	M	70	22	NA
5	TBI*	34	M	68	24.9	2
6	TBI*	31	M	100	26.7	8
7†	TBI‡	55	M	105	28.2	20
8†	MCI¶	71	F	54	23.4	NA
9	MCI§	72	M	83	29.3	NA

*Automobile accident.
†Radiometabolite measurements not performed.
‡NFL multiple concussions.
¶Mini-Mental State Examination = 27.
§Mini-Mental State Examination = 14.
CNTL = control; NA = not applicable.

(kBq/cm^3) measured from the arterial blood samples. Radiometabolite analysis was performed using our automated column-switching radio–high-performance liquid chromatography (radio-HPLC) system (*23,24*). In short, arterial plasma was injected onto the column-switching radio-HPLC and initially trapped on a catch column (Oasis HLB, 30 μm; Waters) using a mobile phase consisting of 99/1 H_2O/MeCN at 1 mL/min (515 pump; Waters). After 4 min, the catch column was backflushed with 75/25 0.1 M ammonium formate/MeCN at 1 mL/min (second Waters 515 pump) and directed onto an XBridge BEH C18 (Waters; 130 Å, 3.5 μm, 4.6 × 100 mm) analytic column. Eluent was collected in 1-min intervals and subsequently assayed for radioactivity using a Wizard 1470 γ-counter (Wallac). After background radioactivity subtraction, radioactivity eluting in the ^{18}F-T807 peak was divided by the total activity and multiplied by 100% for calculation of percentage parent in plasma (%PP).

SUV time courses of radioactivity in whole blood were generated for intersubject comparison by correcting absolute radioactivity concentrations (C [kBq/mL]) for subject body weight (BW [kg]) and injected dose (ID [MBq]): SUV = C/(ID/BW). All subjects underwent arterial sampling for measurement of radioactivity concentration, but because of technical problems, metabolite analysis was not performed in 2 subjects (subjects 7 and 8). Because metabolite analysis was not performed in 2 subjects, %PP time course for all subjects was fit to a single exponential decay to generate a groupwise %PP(t). Individual subject arterial input functions of ^{18}F-T807 radioactivity concentration in plasma were generated by correcting individual plasma radioactivity concentration for ^{18}F-T807 metabolism using the groupwise %PP(t) $C_P(t) = C_P^{total}(t) \times \%PP(t)/100\%$. Finally, ^{18}F-T807 arterial SUV time courses were generated for intersubject comparisons.

Compartmental Modeling with Plasma Input Functions. Compartmental modeling was performed, using in-house–developed software (MATLAB), for estimation of V_T and other kinetic parameters using $C_P(t)$ as the input function. Analyses were implemented on a regional basis using the conventional 1- and 2-tissue-compartment models with a fixed vascular fraction ($f_V = 0.07$) (1T, 2T) or a variable f_V (1Tv, 2Tv) considered an additional parameter (*25*). For completeness, 2-tissue-compartment models with irreversible binding (2T-irrev, 2Tv-irrev)—that is, with the binding dissociation rate constant k_4 set to zero—were also examined.

For models with reversible binding, the outcome of primary interest was the macroparameter V_T, reflecting the equilibrium ratio of radiotracer concentration in the tissue versus plasma (*25*). For 1-tissue models, the V_T is expressed in terms of estimated kinetic parameters by $V_T = K_1/k_2$; for 2-tissue models, the relationship is given by $V_T = (K_1/k_2)(1 + k_3/k_4)$.

Graphical Analysis with Plasma Input Functions. Graphical methods with plasma input functions are alternative techniques for estimation of V_T in which linear regression is applied to an integral transformation of the measured dynamic data. We investigated Logan graphical method (*26*) and multilinear analysis 1 (MA1) (*27*) in this work. The optimal choice for the cutoff time t^* was assessed empirically by repeating analyses for a range of t^* values (20–110 min in 5-min increments) and then assessing the time stability of V_T estimates as well as visually examining the quality of the resulting line fits to determine the earliest cutoff time that was applicable for all subjects and regions measured.

Reference Region–Based Analyses. Reference region–based analyses of ^{18}F-T807 uptake were performed using the cerebellum (excluding the vermis) as a reference tissue. Distribution volume ratio (DVR) (equivalent to V_T/nondisplaceable distribution volume, assuming a valid reference tissue) was estimated using the Logan graphical method with a reference region input function (*28*). The optimal t^* was determined as for the plasma Logan method by systematically varying the cutoff time and assessing linearity of the transformed data and stability of resulting DVR estimates.

The most simplified analysis method surveyed in this work was the SUVR, which is radioactivity concentration in a tissue region divided by the radioactivity concentration in the reference tissue. The cerebellum was again used as the reference tissue, and SUVR was calculated from PET data acquired 80–100 min after injection ($SUVR_{80–100}$).

Estimates of Logan DVR and SUVR were compared with equivalents of DVR from compartmental modeling with arterial inputs, namely V_T^{tissue}/V_T^{ref}.

Parametric Mapping. Dynamic PET images were smoothed by application of a 3-mm (full width at half maximum) gaussian filter. Logan analysis with plasma input was then applied in a voxel-by-voxel fashion to produce parametric maps of V_T^{tissue}/V_T^{ref} to allow a comparison with voxelwise parametric images generated using the Logan method with reference tissue input and static $SUVR_{80–100}$.

Statistical Analysis

The goodness of fit for alternative compartmental models was compared within each dataset using the Akaike information criterion, $AIC = n\ln(RSS/n) + 2k$, where n is the number of time frames, RSS is the residual sum of squares, and k is the number of model parameters (*29*). We used AIC weights to assign to each evaluated model the probability that, out of the set of models considered, that particular model is the correct one, given the data. Weights were calculated as $AIC_{weight,i} = e^{-\frac{1}{2}\Delta_i} / \sum_k e^{-\frac{1}{2}\Delta_k}$, where i indicates the individual model and k indicates the total number of models considered (6, in our case) and $\Delta_i = AIC_i - AIC_{min}$ with AIC_{min} defined as the minimum AIC value for the time–activity curve being evaluated (*30*). To enable group comparison of model preference, median AIC weights are reported in this paper. Statistical processing was performed using Prism software (GraphPad Software). Quantification methods of ^{18}F-T807 were compared using the coefficient of determination and t distribution of the Fisher transformation to generate P values for linear regressions. All data are reported as mean ± SD unless otherwise noted.

RESULTS

Imaging Procedures

PET and MR imaging procedures were performed in 9 subjects from 3 status groups. Subject information is shown in Table 1. The mean and SD of the administered mass of ^{18}F-T807 was 1.0 ± 0.5 μg (range, 0.4–2.0 μg). The mean administered activity was 176 ± 23 MBq (range, 121–196 MBq).

Radioactivity in Arterial Blood

Whole-blood–to–plasma radioactivity concentration rapidly reached equilibrium, averaging 0.98 ± 0.04 by 1 min after injection as shown in Figure 1A. The whole-blood radioactivity time course showed consistency across subjects as shown in Figure 1B. A slight increase in whole-blood SUV was observed at about 30 min after injection.

An example radio-HPLC fraction chromatogram for the 15-min sample from a representative subject (subject 6) is shown in Figure 1C. As confirmed by direct injection of an aliquot of the radiotracer onto the system, ^{18}F-T807 began eluting from the column-switching radio-HPLC at 12 min. Figure 1D shows concentration over time of the 3 radioactivity fractions. %PP of ^{18}F-T807 over time was well described by a single exponential fit, with a half-life of 17.0 ± 4.2 min. Mean and SD of %PP time course is shown in Figure 1E.

The ^{18}F-T807 radioactivity concentration time course in plasma is shown in Figure 1F. At 5 min after injection, the average metabolite-corrected plasma data were described well by a biexponential function (half-lives, 2.4 ± 0.5 and 18.1 ± 5.8 min).

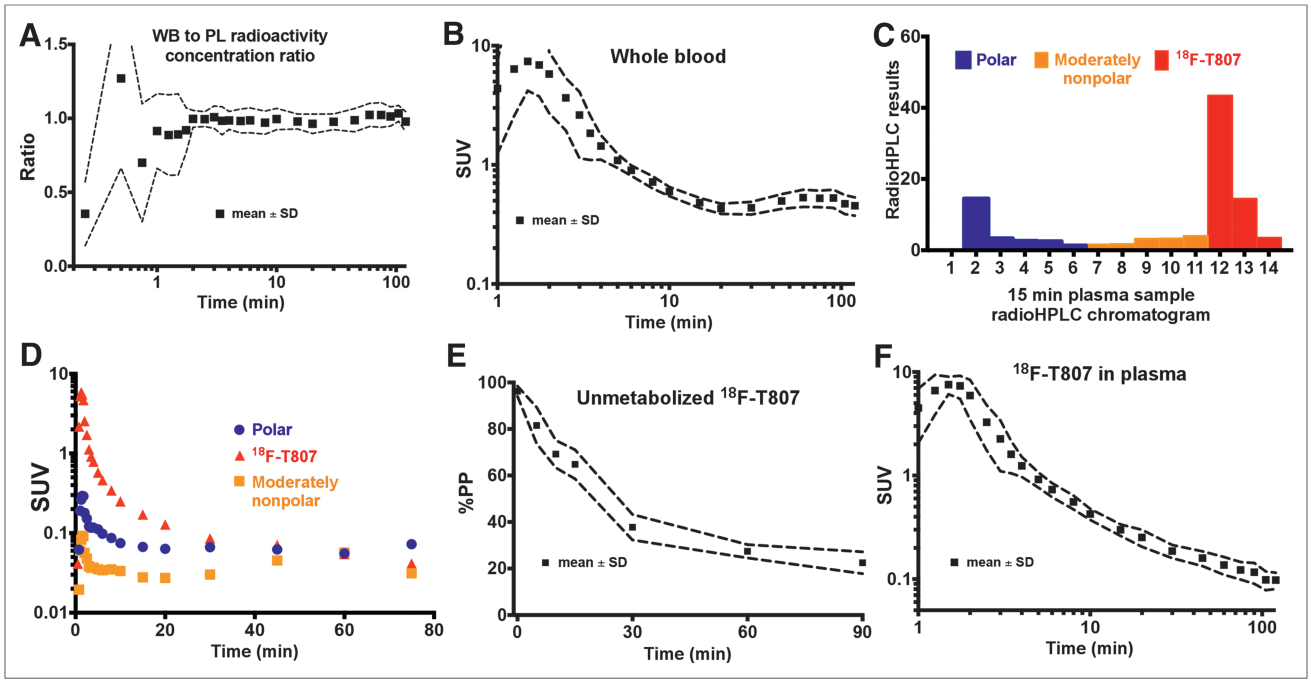

FIGURE 1. Arterial blood measurements. (A) Plot of whole-blood–to–plasma radioactivity concentration ratio. (B) Whole-blood SUV time course. (C) Reversed-phase radio–high-performance liquid chromatogram from 15-min plasma sample in subject 6 with polar, moderately nonpolar, and ^{18}F-T807 components delineated. (D) Time course of polar, slightly nonpolar, and ^{18}F-T807 components as depicted in C. (E) %PP of ^{18}F-T807. (F) ^{18}F-T807 SUV time course in plasma. A, B, E, and F show mean and SD across all subjects, whereas C and D show data from representative subject. PL = plasma; WB = whole blood.

After 10 min, the coefficient of variation in ^{18}F-T807 SUV in plasma across subjects was 17% ± 3.5%. No differences in metabolite-corrected plasma SUV were discernible between subject groups (control, TBI, MCI).

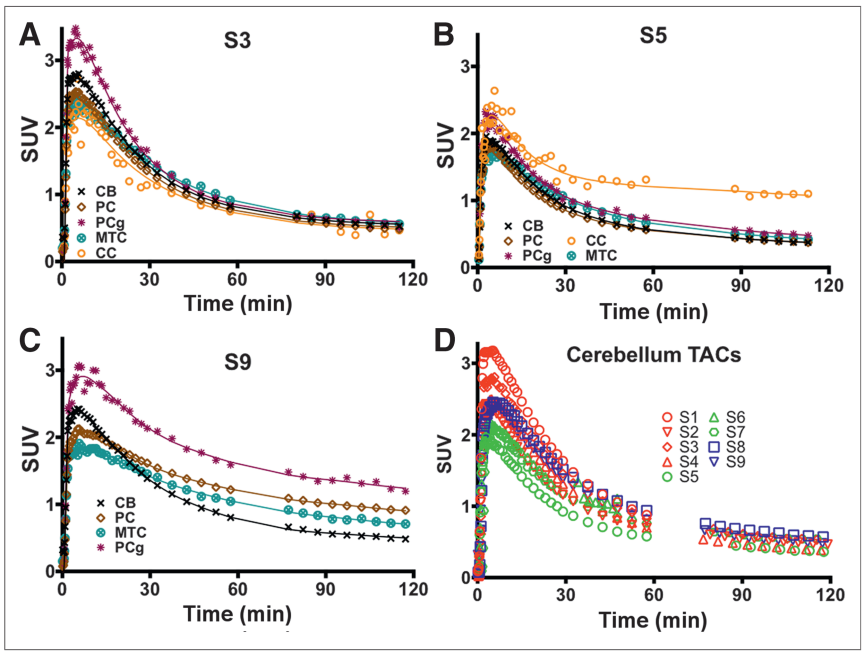

FIGURE 2. (A–C) Time–activity curves and 2Tv (solid lines) fits for a control subject (subject 3), a subject with history of TBI (subject 5), and an MCI subject (subject 9). (D) SUV PET measured time course in cerebellum for all subjects. TAC = time–activity curves.

Region-of-Interest Analysis

SUV_{peak} in gray matter averaged 2.4 ± 0.27 and was greater than 2 for all subjects. In white matter, SUV_{peak} averaged 1.92 ± 0.17 for all subjects. Shown in Figure 2 are regional time–activity curves from different brain regions for a representative control and 2 subjects demonstrating tau pathology. For the control subject, time–activity curves exhibited relatively homogeneous kinetics and converged to similar values by about 40 min. For the 2 subjects demonstrating tau pathology, time–activity curves showed regionally enhanced uptake and greater inter-region heterogeneity in kinetics.

Figure 2D shows cerebellar time–activity curves for all subjects. The cerebellum exhibited fast wash-in of radioactivity with high initial SUV_{peak} (≥2) and rapid clearance (SUV < 1 by 60 min). SUVs reached reasonable convergence by about 60 min. As observed in Figure 2D, subjects with a history of TBI exhibited somewhat reduced SUV_{peak} compared with control and MCI subjects.

Fits to regional time–activity curves for the 2Tv models are shown in Figures 2A–2C (fits for 1Tv models are shown in Supplemental Fig. 2). In MCI subjects, high preference for the 2Tv reversible model was observed ($AIC_{weight,median}$ = 1). In control subjects, preference for the 2Tv

reversible model was maintained with an $AIC_{weight,median} = 0.73$. Interestingly, for the TBI subjects, model preference seemed to shift toward the 2Tv irreversible model, with an $AIC_{weight,median} = 0.05$ for the reversible and $AIC_{weight,median} = 0.48$ for the irreversible model. The 2Tv reversible model was selected as the compartmental method of choice because it provided good fits in all datasets (notably including those showing high uptake), was statistically preferred in most datasets, and provided an outcome consistent with our understanding of the tracer's binding properties. Compartmental results reported throughout the remainder of this paper are derived using this model unless otherwise noted. Omission of the vascular contribution (f_V) as a parameter greatly reduced *AIC* weights ($AIC_{weight,median} = 0$). Regional V_T estimates from the 2Tv model are shown in Figure 3A and Supplemental Table 2. The cerebellum showed the lowest variability in V_T (4.1 ± 0.5; coefficient of variation = 11.8%) despite larger variation in SUV (Fig. 2D and text earlier in this section). No significant differences in cerebellar V_T, K_1, or k_2 were found between the subject groups. Cerebellar K_1 was stable at 0.26 ± 0.06 mL·min^{-1}·cm^{-3}), with higher variability found in k_2 (0.17 ± 0.13 min^{-1}).

Logan (*26*) and MA1 (*27*) graphical methods resulted in estimates of V_T highly correlated with those from 2Tv. The Logan plot for 1 subject with a range of uptake is shown in Figure 3B, demonstrating a reasonable level of linearization by t^* of 30 min. As shown in Figures 3C and 3D, high correlation was found between both graphical methods and the estimates of V_T from compartmental analysis (Logan: $R^2 = 0.97$, $P < 0.0001$; MA1: $R^2 = 0.97$, $P < 0.0001$). Additionally, as shown in Supplemental Figure 3, estimates of Logan V_T correlated well with MA1 V_T (Logan: $R^2 = 0.99$, $P < 0.0001$).

Reference region–based analysis was performed using the cerebellum because of the high consistency observed in V_T across the subjects. Logan analyses performed with t^* systematically varied between 20 and 110 min demonstrated stabilization in DVR over all regions by approximately 55 min. A representative Logan plot is shown in Figure 4A demonstrating that linearization is reached by the 55-min cutoff (indicated by the large circles) even in the higher binding regions. A comparison of 2Tv V_T/V_T^{ref} and Logan DVR is shown in Figure 4B, indicating high correlation ($R^2 = 0.96$, $P < 0.0001$), though with some negative bias at high values. A comparison of 2Tv V_T/V_T^{ref} and $SUVR_{80–100}$ shows similarly high correlation ($R^2 = 0.96$, $P < 0.0001$; Fig. 4C), however, no bias is evident across the range of observed values. In white matter, $SUVR_{80–100}$ averaged 1.15 ± 0.1 over all control subjects.

Figure 5 shows SUVR time courses along with Logan DVR and 2Tv V_T/V_T^{ref} estimates for 3 regions in 1 control subject and 1 MCI subject. The control subject reached a plateau in all regions within about 20 min. In the higher uptake regions of the MCI subject, a plateau began by approximately 80–90 min.

^{18}F-T807 Parametric Images

^{18}F-T807 Logan V_T^{tissue}/V_T^{ref}, Logan DVR, and $SUVR_{80–100}$ maps generated using the cerebellum as a reference region are shown in Figure 6 for 1 control subject, 1 subject who had been in an automobile accident approximately 2 y before imaging with ^{18}F-T807, and 2 MCI subjects. Also displayed is the subject's MPRAGE image in standardized space of the same slice for localization. Overall features are comparable for the alternative PET analysis methods; however, some discrepancies can be observed. For instance, $SUVR_{80–100}$ has a generally noisier appearance and exhibits relatively higher signal in white matter than either of the kinetic analysis methods, a phenomenon most prominent in the control and TBI subjects. Conversely, signal in the basal ganglia is reduced in the $SUVR_{80–100}$ images as compared with maps obtained by Logan regression methods; similar patterns are present elsewhere, notably in the occipital lobe of one MCI subject (subject 8) and in the frontal cortex of the other (subject 9).

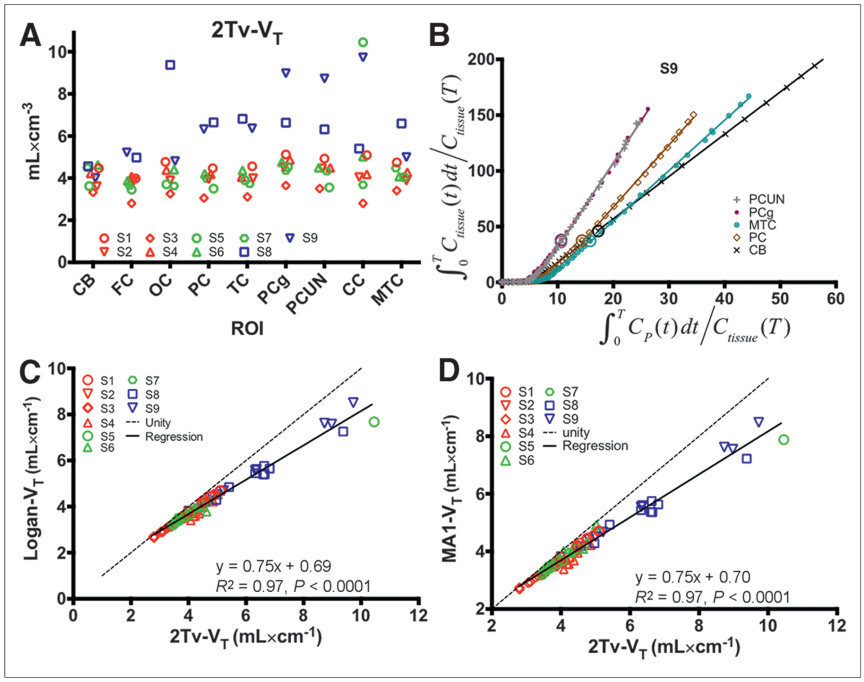

FIGURE 3. Results from arterial input function–based analyses. (A) Regional V_T estimates from 2Tv compartmental model in cerebellum (CB), frontal cortex (FC), occipital cortex (OC), parietal cortex (PC), temporal cortex (TC), posterior cingulate gyrus (PCg), precuneus (PCUN), subject-specific region of interest (ROI) in corpus callosum (CC), and mesial temporal cortex (MTC). (B) Demonstration of Logan plot linearization in MCI subject (subject 9) for estimation of V_T. Large circles depict 30-min t^* point. Axes were truncated to enhance visualization of higher binding regions. (C and D) Comparison of 2Tv and graphical estimates of V_T using either Logan analysis (C) or MA1 (D). In A, C, and D, red markers designate control subjects, green markers correspond to TBI subjects, and blue markers indicate MCI subjects.

DISCUSSION

There has been a great effort toward the development of PET imaging agents for tau pathology because of the implication of tau in neurodegenerative diseases such as Alzheimer disease and TBI. ^{18}F-T807 was developed for PET imaging of tau pathology. It has been widely used in research studies and is currently undergoing clinical trials as a diagnostic PET radiotracer. Despite its expanding use, a full characterization of ^{18}F-T807's pharmacokinetics has yet to be investigated. The goal of this

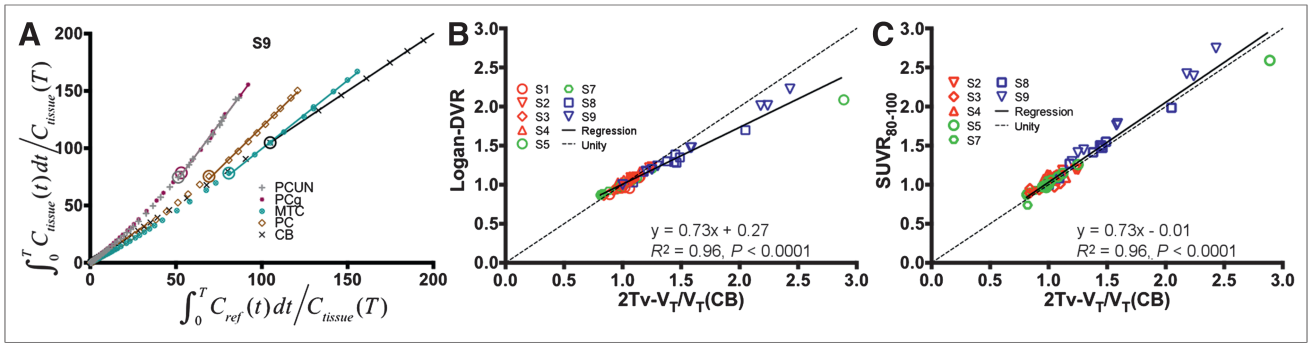

FIGURE 4. Results from reference region–based analyses with cerebellar input functions. (A) Demonstration of Logan plot linearization in MCI subject (subject 9) for estimation of DVR. Large circles depict 55-min t^* point. Axes were scaled down to enhance visualization of higher uptake regions. Comparison of Logan DVR (B) and $SUVR_{80–100}$ (C) against indirect calculations of DVR given V_T/V_T^{ref} with distribution volumes estimated by compartmental modeling with arterial input functions and V_T^{ref} corresponding to cerebellum. CB = cerebellum; PC = parietal cortex; PCg = posterior cingulate gyrus; PCUN = precuneus; MTC = mesial temporal cortex.

work was to provide an initial in vivo pharmacokinetic evaluation of the tau radiotracer ^{18}F-T807 using metabolite-corrected arterial input functions and dynamic PET imaging data. Herein, we evaluate subjects who present a range of ^{18}F-T807 uptake to properly assess different methods for quantification and to provide a preliminary analysis of simplified reference region–based methods.

^{18}F-T807 in Blood

Radioactivity concentration in whole blood demonstrated rapid clearance, with approximately 4% of the initial peak radioactivity present at 20 min after injection. Nonpolar radioactive metabolites detected using radio-HPLC were minimal. Furthermore, high intersubject consistency was found in ^{18}F-T807 metabolism, and ^{18}F-T807 breakdown resulted primarily in polar metabolites. For this analysis, we found a group %PP function to be adequate because of the high similarity in ^{18}F-T807 metabolism between subjects as the group %PP versus subject-specific %PP correction resulted in highly concordant estimates of V_T as shown in Supplemental Figure 4 ($R^2 = 0.99,\ y = 1.02x - 0.09, P < 0.0001$).

Cerebellum as Reference Region

For simplified quantification methods beyond SUV, a reference region void of radiotracer target is necessary to provide a surrogate for the arterial input function. Of the regions examined in this work, the cerebellum showed the lowest variability in V_T and the lowest overall V_T. Additionally, the cerebellum showed fast wash-in and fast clearance, resulting in low overall specific binding of ^{18}F-T807. In the control and TBI subjects, some regions exhibited DVR values < 1; however, regional DVRs in MCI subjects were ≥ 1. Other potential reference regions examined in this work included parts of the brain stem comprising the pons and medulla; however, high variability in V_T was found in these areas. This preliminary analysis supports the use of the cerebellum as the most appropriate reference region. Because of the particular staging of tau in Alzheimer disease, we do not anticipate that the cerebellum will comprise significant tau deposition (*17,31,32*). Subjects with TBI, on the other hand, could potentially present with tau in a less predictable manner. Ultimately, a larger study set will be required to fully validate the cerebellum as a reference region in Alzheimer disease subjects and subjects with TBI.

Simplified Approaches for Quantification of ^{18}F-T807 Uptake

We examined simplified approaches for quantification of ^{18}F-T807 uptake including the Logan method for estimation of DVR and SUVR. High correlation was observed between compartmental modeling–based estimates of V_T/V_T^{ref} using the cerebellum as a reference and estimates of Logan DVR and SUVR indicating reference region–based estimates of ^{18}F-T807 uptake will be an adequate alternative to full arterial sampling and compartmental modeling. Examination of truncated imaging times on Logan DVR estimation showed that results from 90 min of data were comparable to those from 120 min, whereas 60 min of data yielded biases of $> 10\%$. SUVR overestimated V_T/V_T^{ref} when compared with the Logan DVR method; however, reasons for this overestimation have been discussed in the literature (*33,34*). Plots of SUVR time course suggested at least 80–100 min of time would be required for high ^{18}F-T807 binding regions to reach pseudoequilibrium with the reference region, which is similar to previously suggested SUVR imaging times (*12*). Comparison of SUVR maps using 40–60 min, 80–100 min, and 100–120 min are shown in Supplemental Figure 5. As demonstrated, SUVRs from 80–100 min and 100–120 min are comparable, but SUVRs from 40 to 60 have not reached

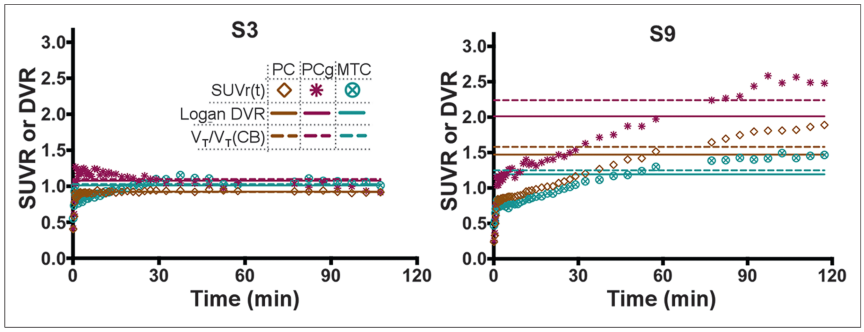

FIGURE 5. SUVR time courses (symbols), DVR estimated directly by Logan regression with reference region inputs (horizontal solid lines), and DVR estimated indirectly by V_T/V_T^{ref} from compartmental modeling with arterial inputs (horizontal dashed lines) for control subject (subject 3) and MCI subject (subject 9). CB = cerebellum; PC = parietal cortex; PCg = posterior cingulate gyrus; MTC = mesial temporal cortex.

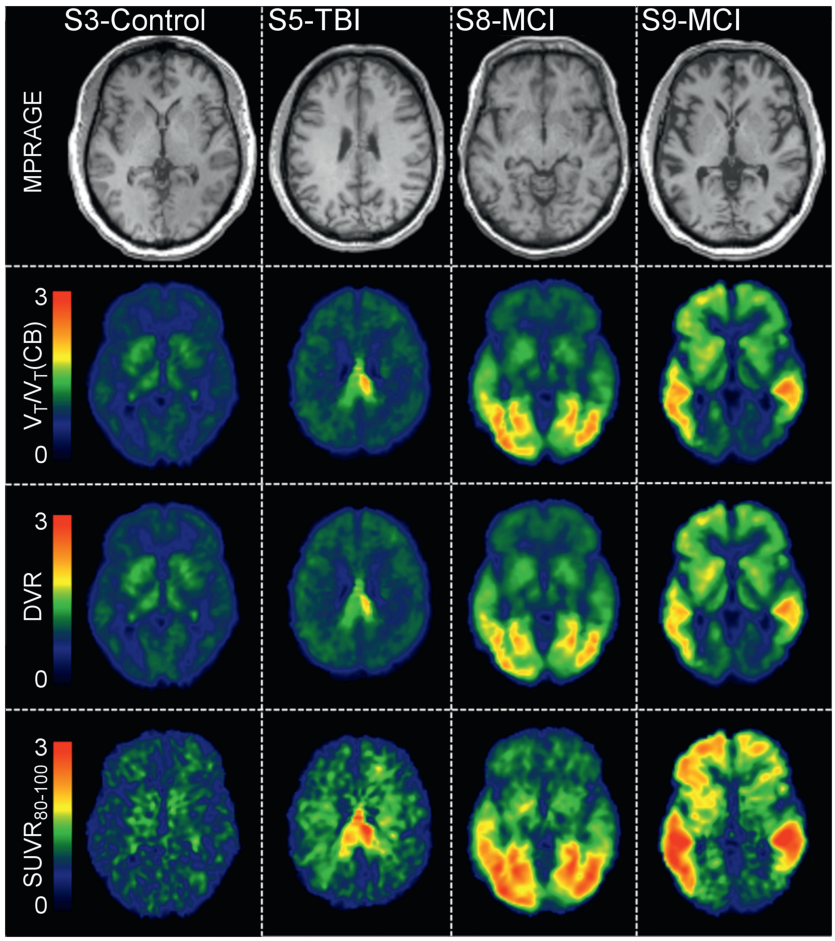

FIGURE 6. MPRAGE in template space and parametric images of indirect calculation of DVR using Logan (V_T/V_T(CB)), Logan DVR, and SUVR in control subject (subject 3), a subject with history of TBI (subject 5), and 2 subjects with MCI (subjects 8 and 9).

peak values. In the lower binding subjects and regions, however, about 30 min are necessary for SUVR to become stable. These results provide compelling evidence that late static imaging may serve in place of full dynamic imaging with arterial blood sampling.

^{18}F-T807 Uptake and Distribution

^{18}F-T807 demonstrated high brain penetration, with an SUV_{peak} immediately after injection of greater than 2 in gray matter. Additionally, K_1 averaged 0.25 across subjects and regions, indicating moderately high brain extraction. Previous work has shown THK5105 to have high nonspecific white matter binding (*11*). This nonspecific uptake is attributed to β-sheet structures in myelin and could be problematic for quantification of tau. SUV_{peak} of ^{18}F-T807 in white matter averaged 1.92 and $SUVR_{80–120}$ min in white matter was 1.15 ± 0.1, indicating mild nonspecific white matter binding. In contrast to ^{18}F-T808, uptake in the skull was minimal for ^{18}F-T807 (Supplemental Fig. 6), indicating low defluorination.

As the parametric images in Figure 6 indicate, ^{18}F-T807 uptake can be quantified reliably using graphical methods or SUVR. Images of SUVR were the lowest quality, with apparent uptake in white matter that was not observed in the V_T or DVR maps; however, SUVR seemed to be adequate for delineation and estimation of relative uptake of ^{18}F-T807.

Overall, distribution of ^{18}F-T807 in the control subjects was generally uniform, with no cortical areas expressing high distribution. Although not explicitly examined in this work, intersubject heterogeneity in uptake was observed in subcortical areas, for example, the thalamus and putamen. Similar off-target binding results have been observed (*35*). In addition, our previous autoradiography work demonstrated off-target binding to neuromelanin- and melanin-containing cells as well as hemorrhagic lesions (*17*). Further examination of this off-target subcortical binding is warranted. The subject with a severe TBI due to an automobile accident expressed 1 region of high uptake protruding from the posterior regions of the corpus callosum into the posterior cingulate gyrus, possibly as a result of brain injury. Finally, the 2 MCI subjects demonstrated different distributions in uptake. Subject 8 had highest uptake in the occipital regions. Subject 9, on the other hand, demonstrated high ^{18}F-T807 uptake in areas associated with staging of tau in Alzheimer disease (*31*) including temporal, parietal, posterior cingulate, and precuneus regions.

This work had some limitations, including no test–retest data. However, we observed low variability in blood data and cerebellar V_T across subjects, indicating test–retest variability would also be low. Use of a groupwise ^{18}F-T807 metabolism correction is a limitation, and a full examination of intersubject variability in ^{18}F-T807 metabolism would be helpful to determine whether differences exist between groups (MCI, TBI, and controls). Additionally, we examined only tauopathies related to MCI subjects and subjects with history of brain injury. A thorough investigation of ^{18}F-T807 kinetics in subjects with related tauopathies (e.g., frontotemporal dementia) will be necessary to determine whether the ^{18}F-T807 kinetic properties found in this work translate to other tau-related diseases. Even though for most subjects a 2-tissue-reversible model was preferred based on *AIC,* we found preference for the irreversible model in our TBI subjects. A full examination of ^{18}F-T807 kinetics in TBI subjects with a range of binding is needed to investigate this apparent discrepancy. Finally, our overall subject number was low; however, the subjects examined in this work had a wide range of dynamic ^{18}F-T807 uptake, allowing evaluation of ^{18}F-T807's kinetics in subjects with the highest binding expected as indicated by Johnson et al. who found highest ^{18}F-T807 posterior cingulate SUVRs between 2 to 2.5 (*18*).

CONCLUSION

^{18}F-T807 showed low intersubject variability in metabolism rate and overall rapid clearance in plasma. Two-tissue-reversible compartmental modeling using ^{18}F-T807 arterial input function resulted in close agreement with linearized methods of

V_T estimation using both Logan (*26*) and MA1 (*27*). The cerebellum exhibited properties required for use as a reference region in place of arterial sampling. These initial results show promise for a simplified reference region–based protocol, negating arterial sampling and using late static imaging with the goal of shorter scan times. Reference region–based methods of quantification including Logan DVR with a $t^* = 55$ min and SUVR from 80 to 100 min tracked closely with compartmental modeling based outcome measures using arterial plasma input functions. Lastly, these results demonstrate that ^{18}F-T807 possesses the properties necessary for quantification of tau using PET imaging. Further studies will be needed to fully characterize the use of the cerebellum as a valid reference region in a heterogeneous population.

DISCLOSURE

No potential conflict of interest relevant to this article was reported.

REFERENCES

1. Iqbal K, Liu F, Gong CX, Grundke-Iqbal I. Tau in Alzheimer disease and related tauopathies. *Curr Alzheimer Res.* 2010;7:656–664.
2. James OG, Doraiswamy PM, Borges-Neto S. PET imaging of tau pathology in Alzheimer's disease and tauopathies. *Front Neurol.* 2015;6:38.
3. Hyman BT, Phelps CH, Beach TG, et al. National Institute on Aging-Alzheimer's Association guidelines for the neuropathologic assessment of Alzheimer's disease. *Alzheimers Dement.* 2012;8:1–13.
4. Goldstein LE, Fisher AM, Tagge CA, et al. Chronic traumatic encephalopathy in blast-exposed military veterans and a blast neurotrauma mouse model. *Sci Transl Med.* 2012;4:134ra60.
5. McKee AC, Cantu RC, Nowinski CJ, et al. Chronic traumatic encephalopathy in athletes: progressive tauopathy after repetitive head injury. *J Neuropathol Exp Neurol.* 2009;68:709–735.
6. Ariza M, Kolb HC, Moechars D, Rombouts F, Andres JI. tau positron emission tomography (PET) imaging: past, present, and future. *J Med Chem.* 2015;58: 4365–4382.
7. Agdeppa ED, Kepe V, Liu J, et al. Binding characteristics of radiofluorinated 6-dialkylamino-2-naphthylethylidene derivatives as positron emission tomography imaging probes for beta-amyloid plaques in Alzheimer's disease. *J Neurosci.* 2001;21:RC189.
8. Hashimoto H, Kawamura K, Igarashi N, et al. Radiosynthesis, photoisomerization, biodistribution, and metabolite analysis of ^{11}C-PBB3 as a clinically useful PET probe for imaging of tau pathology. *J Nucl Med.* 2014;55:1532–1538.
9. Kimura Y, Ichise M, Ito H, et al. PET quantification of tau pathology in human brain with ^{11}C-PBB3. *J Nucl Med.* 2015;56:1359–1365.
10. Harada R, Okamura N, Furumoto S, et al. ^{18}F-THK5351: a novel PET radiotracer for imaging neurofibrillary pathology in Alzheimer's disease. *J Nucl Med.* 2016; 57:208–214.
11. Okamura N, Furumoto S, Fodero-Tavoletti MT, et al. Non-invasive assessment of Alzheimer's disease neurofibrillary pathology using ^{18}F-THK5105 PET. *Brain.* 2014;137:1762–1771.
12. Chien DT, Bahri S, Szardenings AK, et al. Early clinical PET imaging results with the novel PHF-tau radioligand [F-18]-T807. *JAD.* 2013;34:457–468.
13. Xia C-F, Arteaga J, Chen G, et al. [^{18}F]T807, a novel tau positron emission tomography imaging agent for Alzheimer's disease. *Alzheimers Dement.* 2013;9:666–676.
14. Zhang W, Arteaga J, Cashion DK, et al. A highly selective and specific PET tracer for imaging of tau pathologies. *JAD.* 2012;31:601–612.
15. Chien DT, Szardenings AK, Bahri S, et al. Early clinical PET imaging results with the novel PHF-tau radioligand [F18]-T808. *J Alzheimers Dis.* 2014;38:171–184.
16. Shoup TM, Yokell DL, Rice PA, et al. A concise radiosynthesis of the tau radiopharmaceutical, [^{18}F]T807. *J Labelled Comp Radiopharm.* 2013;56:736–740.
17. Marquié M, Normandin MD, Vanderburg CR, et al. Validating novel tau positron emission tomography tracer [F-18]-AV-1451 (T807) on postmortem brain tissue. *Ann Neurol.* 2015;78:787–800.
18. Johnson KA, Schultz A, Betensky RA, et al. Tau PET imaging in aging and early Alzheimer's disease. *Ann Neurol.* 2016;79:110–119.
19. Brant-Zawadzki M, Gillan GD, Nitz WRMP. RAGE: a three-dimensional, T1-weighted, gradient-echo sequence–initial experience in the brain. *Radiology.* 1992;182:769–775.
20. Alpert NM, Berdichevsky D, Levin Z, Morris ED, Fischman AJ. Improved methods for image registration. *Neuroimage.* 1996;3:10–18.
21. Grabner G, Janke AL, Budge MM, Smith D, Pruessner J, Collins DL. Symmetric atlasing and model based segmentation: an application to the hippocampus in older adults. *Med Image Comput Comput Assist Interv.* 2006;9(Pt 2):58–66.
22. Jenkinson M, Beckmann CF, Behrens TEJ, Woolrich MW, Smith SM. FSL. *Neuroimage.* 2012;62:782–790.
23. Collier T, Normandin M, El Fakhri G, Vasdev N. Automation of column-switching HPLC for analysis of radiopharmaceuticals and their metabolites in plasma [abstract]. *J Nucl Med.* 2013;54:1133.
24. Hilton J, Yokoi F, Dannals RF, Ravert HT, Szabo Z, Wong DF. Column-switching HPLC for the analysis of plasma in PET imaging studies. *Nucl Med Biol.* 2000;27:627–630.
25. Innis RB, Cunningham VJ, Delforge J, Fujita M, Gjedde A, Gunn RN. Consensus nomenclature for in vivo imaging of reversibly binding radioligands. *J Cereb Blood Flow Metab.* 2007;27:1533–1539.
26. Logan J, Fowler JS, Volkow ND, et al. Graphical analysis of reversible radioligand binding from time-activity measurements applied to [N-^{11}C-methyl]-(-)-cocaine PET studies in human subjects. *J Cereb Blood Flow Metab.* 1990;10:740–747.
27. Ichise M, Toyama H, Innis RB, Carson RE. Strategies to improve neuroreceptor parameter estimation by linear regression analysis. *J Cereb Blood Flow Metab.* 2002;22:1271–1281.
28. Logan J, Fowler JS, Volkow ND, Wang GJ, Ding YS, Alexoff DL. Distribution volume ratios without blood sampling from graphical analysis of PET data. *J Cereb Blood Flow Metab.* 1996;16:834–840.
29. Akaike H. A new look at the statistical model identification. *IEEE Trans Automat Contr.* 1974;19:716–723.
30. Burnham KP, Anderson DR, Burnham KP. *Model Selection and Multimodel Inference: A Practical Information-Theoretic Approach.* 2nd ed. New York, NY: Springer; 2002.
31. Braak H, Braak E. Neuropathological stageing of Alzheimer-related changes. *Acta Neuropathol (Berl).* 1991;82:239–259.
32. McKee AC, Stern RA, Nowinski CJ, et al. The spectrum of disease in chronic traumatic encephalopathy. *Brain.* 2013;136:43–64.
33. Slifstein M. Revisiting an old issue: the discrepancy between tissue ratio-derived binding parameters and kinetic modeling-derived parameters after a bolus of the serotonin transporter radioligand ^{123}I-ADAM. *J Nucl Med.* 2008;49:176–178.
34. Carson RE, Channing MA, Blasberg RG, et al. Comparison of bolus and infusion methods for receptor quantitation: application to ^{18}F-cyclofoxy and positron emission tomography. *J Cereb Blood Flow Metab.* 1993;13:24–42.
35. Shcherbinin S, Schwarz AJ, Joshi AD, et al. Kinetics of the tau PET tracer ^{18}F-AV-1451 (T807) in subjects with normal cognitive function, mild cognitive impairment and Alzheimer's disease. *J Nucl Med.* 2016;57:1535–1542.